RESEARCH ON INFRARED ALARM OPTICAL SYSTEM WITH LARGE FIELD OF VIEW

Zhigang LI[1], Junhua ZHOU[2], Dangshe QIU[3], Sichao SU[1], Duhang LI[4, *]

In response to the real-time perception requirements of the entire spatial domain, this study innovatively designed an infrared warning optical system with a large field of view. Combining an inverse distant objective lens and an equidistant projection model with negative distortion compensation (distortion ≤2%) and optical focal optimization, it achieved an ultra-wide field of view of 120.6°×95.8° on a 16mm×12.8mm image plane (an increase of 38% compared to the traditional approach). The system adopts a lightweight aluminum alloy barrel and a primary imaging architecture, with a wide temperature range adaptive capability (focal shift <5μm from -40 to 60 ° C), 100% cold diaphragm efficiency, >80% edge illuminance, 5G vibration resistance. The reliability is improved by a sealing process. This solution breaks through the field of view and temperature drift limitations of traditional infrared systems, providing a cost-effective omnidirectional sensing solution for airborne/vehicle-mounted platforms.

Key words: Large field of view infrared warning system, reverse long-range objective lens structure, negative distortion compensation, wide temperature range adaptive

1. Introduction

With the development of modern warfare to informatization and intelligence, infrared warning systems have become one of the core equipment for battlefield situation awareness and defense systems due to their strong concealment and anti-electromagnetic interference capabilities [1]. The wide-field infrared warning system can achieve all-round real-time surveillance of the airspace in all directions by expanding the detection coverage, significantly enhancing the early warning capability for low-altitude fast targets such as missiles and unmanned aircrafts. Compared with multi rotor drones, unmanned helicopter has stronger payload capacity and prolonged operational duration, thereby alleviating design constraints related to spectrometer weight, physical dimensions, and energy

[1]School of Mechanical Engineering, Hunan University of Arts and Science, Changde 415000, China
[2]The 27th Research Institute of China Electronics Technology Group Corporation, Henan, 450047, China
[3]Hunan South China Optoelectronics (Group) Co., Ltd., Hunan, 415005, China
[4]University of New South Wales, Sydney, New South Wales, Australia
[*]985418363@qq.com

requirements [2]. Over the last decades, unmanned aerial vehicles have impacted many military applications and public services [3]. Fang et al. [4] devised and implemented a high-speed, wide-field mid-infrared hyperspectral imaging system based on broadband parametric up-conversion of high-brightness super continuum illumination in the Fourier plane. However, although the wide field of view design improves the detection range, it also faces technical challenges such as complex background interference, low signal-to-noise ratio of small and weak targets, and high-speed data transmission and processing. Progress has been made in improving target detection accuracy and system stability through multi-band fusion, thermal design of optical systems, and adaptive filtering algorithms. Conventional tri-band infrared optical systems aim to simultaneously image short-wave (SWIR), mid-wave (MWIR), and long-wave (LWIR) spectral regions, have historically relied on prismatic or diffraction-based spectral separation mechanisms. This fundamental design paradigm inevitably introduces critical limitations, including excessive size/weight penalties, cascaded optical path complexity, suboptimal photon utilization efficiency, and compromised scalability for rapid field deployment [5]. Choi et al. [6] introduced a series of optical analysis techniques that span different disciplines, with a focus on boundary condition modification, fast multipole methods, coupled mode theory, and neural network-based methods. Li et al. [7] designed an ultra-low self-heating radiation long-wave infrared laser communication optical system. The system includes an aperture stop, a primary mirror, a secondary mirror, a three-mirror assembly, a field stop, a four-mirror assembly, a protective window glass, a detector light shield, and an image plane. The configuration aims to optimize optical performance while minimizing thermal radiation and self-heating effects for long-wave infrared applications. The key technical bottlenecks of wide-field infrared warning systems are studied, and optical design and intelligent algorithm optimization are combined to explore their high-precision target positioning and low false alarm rate detection capabilities in complex battlefield environments, providing theoretical support and technical reference for the development of the next generation of infrared warning equipment.

2. Basic principles

Real-time monitoring of the 360° peripheral airspace is carried out. To avoid blind spots in the field of view splicing and reduce the overlap rate of the field of view, it is necessary to reasonably select the field of view of a single optical system. Fig. 1 shows the layout of a field of view, where a single optical lens needs to cover a field of view area of ≥94°×94°, and the field of view overlap between adjacent lenses is ≥4°, achieving full coverage of the 4π spherical space through the combination of 6 optical lenses. The large field of view infrared warning system

can achieve all-round real-time monitoring of the airspace by expanding the detection coverage, significantly enhancing the early warning capability for low-altitude fast targets.

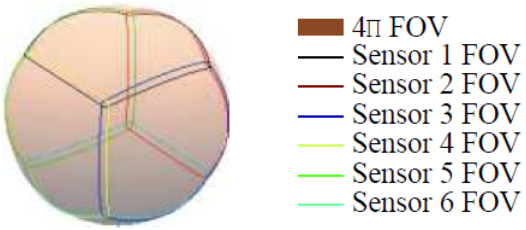

Fig. 1. Layout of the optical lens field of view

For object imaging at infinity, the image height and field of view of an ideal optical lens with zero image distortion conforming to the following formula:

$$h = f \tan\theta \tag{1}$$

where: f is the object side focal length, and θ is the object side half-field of view Angle.

The core of the principle of similarity imaging is to follow the similarity between objects and images, satisfy the Gaussian optical conjugate relationship, and generally classify field of view lenses in engineering as follows:

$$2\theta > 120°$$
$$80° \le 2\theta \le 120°$$
$$60° \le 2\theta < 80°$$
$$45° \le 2\theta < 60°$$

When the angle 2θ is greater than 120°, it is classified as a fisheye lens; When the angle is $80° \le 2\theta \le 120°$, it is classified as an ultra wide angle lens; When the angle is $60° \le 2\theta < 80°$, it is classified as a wide-angle lens; When the angle is $45° \le 2\theta < 60°$,it is classified as a standard lens.

According to the trigonometric function in formula (1), the principle of similar imaging is generally applicable to small field of view, such as standard lenses, telephoto lenses, etc. When the field of view is ≥90°, the image height will sharply increase, and the $\tan\theta$ value is no longer reasonable. Optical systems including ultra wide angle lenses and fisheye lenses cannot image in a limited image plane. Therefore, the ideal image height formula does not conform to practical applications. Ultra large field of view optical lenses must introduce a certain amount of negative distortion in order to design a sufficient imaging field of view in a limited image plane size. When the field of view angle is too large, non similar imaging principles are often used for design.

In engineering, in order to obtain real-time information in the angular space that cannot be imaged according to the principle of similar imaging (Gaussian optics), implementing "deformation compression" on the object space is the only feasible method.

The core of the principle of dissimilar imaging is to actively introduce barrel distortion and compress the object's large field of view to a finite image plane through nonlinear projection. There are usually several formulas that meet the conditions for wide-angle design [8-10]:

$$h = 2f\tan(\theta/2) \tag{2}$$

$$h = 2f\sin(\theta/2) \tag{3}$$

$$h = f\sin\theta \tag{4}$$

$$h = f\theta \tag{5}$$

In the above formula, h is the image height, f is the focal length, and θ is the field of view angle. Formula 1 is the ideal pinhole camera model, and most ordinary lenses (small to medium field of view) will produce significant distortion at wide angles. Formula (2) is a stereoscopic projection, expressed as equal radial and tangential magnification, with spherical objects imaged as similar circles, suitable for classical wide-angle lens designs; Formula (3) is equal solid angle projection, expressed as the solid angle of the object is proportional to the area of the image plane, suitable for solid angle measurement, such as meteorological observation, panoramic photography, etc; Formula (4) is an orthogonal projection, expressed as extreme compression of the edge field of view, with the radial magnification of the edge field of view approaching zero and the maximum distortion, suitable for special scenarios such as pipeline inspection; Formula (5) is an equidistant projection, expressed as a linear correlation between image height and field of view angle, suitable for real-time target positioning, such as warning systems, missile tracking, etc.

The imaging image height and field of view usually conform to the following projection method, and the angular resolution is defined as the ratio $dh/d\theta$ of the change in image height to the change in field of view angle, reflecting the number of pixels corresponding to a unit field of view angle (the smaller the resolution, the higher the resolution).

Therefore, by taking the derivatives on both sides of the above formulas (1)-(5), the relationship between angular resolution and field of view is obtained as follows, and the applicability of formulas (6)-(10) is the same as that of formulas (1)-(5):

$$dh/d\theta = f/\cos(\theta)^2 \tag{6}$$

$$dh/d\theta = f/\cos(\theta/2)^2 \tag{7}$$

$$dh/d\theta = f\cos(\theta/2) \tag{8}$$

$$dh/d\theta = f\cos(\theta) \tag{9}$$

$$dh/d\theta = f \tag{10}$$

The relationship between the image height and the field of view Angle corresponding to different projection methods is shown in Fig. 2 (a). The relationship between the angular resolution and the field of view Angle corresponding to different projection methods is shown in Fig. 2 (b).

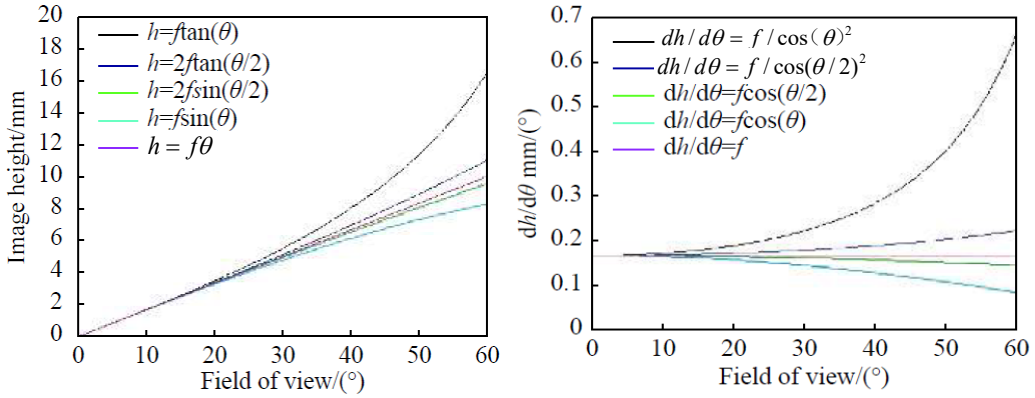

(a) (b)

Fig.2 (a) The relationship between image height and field of view; (b) The relationship between angular resolution and field of view

An ordinary photographic lens usually has a rear intercept of 0.6 to 0.8 times the focal length. Sometimes it is required that the rear intercept be long enough to accommodate other optical elements, especially for the short focal length structure, which requires an inverse telephoto structure to meet such requirements, as shown in Fig. 3.

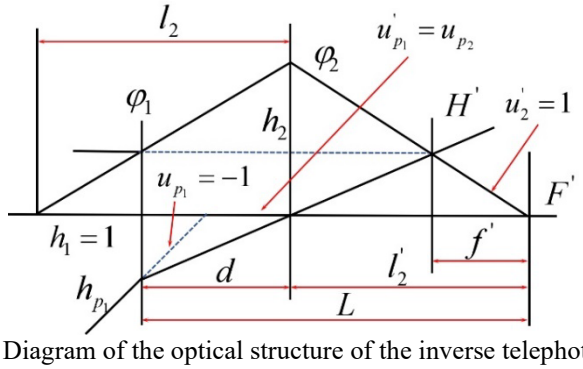

Fig. 3 Diagram of the optical structure of the inverse telephoto type

φ_1 and φ_2 represent the optical power of the front and rear groups; h_1 and h_{p1} are the heights of the axial ray and the principal ray in the front group, respectively; u_{p1}, u'_{p1} and u_{p2} are respectively the incident angle of the main ray in the front group, the angle refracted by the front group, and the angle entering the rear group; The exit angle of u'_2 as the main ray refracted by the posterior group; d is the interval between the front and back groups; l_2 and l'_2 are the distances from the front group to the reference plane and from the back group to the reference plane; f' is the focal length of the image square; L is the system length; F' is the focal point of the image square, and H' is the principal point of the image square.

In addition to long back intercept, the anti-telephoto objective lens also needs to meet certain requirements of field of view angle. Off axis light rays diverge through the front group negative lens, causing a rapid decrease in their angle with the optical axis, which is beneficial for correcting off axis aberrations. The inverse to far ratio is l'_2 / f'. If f' is small and l'_2 is large, the inverse to far ratio will be large.

In addition to having a certain rear intercept and field of view, the structure of the anti-distance structure also needs to be as simple and compact as possible. To reduce the volume, the distance between the front and back groups should be reduced.

Assuming the reciprocal of the magnification of the principal ray angle in the previous group is γ_1, it can be deduced that [11-13]:

$$\frac{1}{\gamma_1} = \frac{u_{p_1}}{u_{p_{1'}}} = 1 - d\varphi_1 \tag{11}$$

After γ_1 is determined, if d is to be reduced, φ_1 must be increased, resulting in a complex front image and an increase in the aperture angle borne by the front group. The high-order aberrations related to the aperture will also increase. To reduce the high-order aberrations related to the aperture, it is necessary to complicate the structure. It can be seen that γ_1 plays a dominant role in determining the back intercept and field of view of the anti-telephoto objective lens.

If the front group $1/\gamma_1$ and the field of view angle are larger, the aberrations related to the field of view will also increase, and the distortion will be more severe. Usually, the front group retains a certain amount of distortion to compensate for the distortion of the opposite sign in the back group.

For ultra wide angle systems with a field of view close to 180 °, due to the presence of a large amount of barrel distortion, the relationship between the image

height and the field of view angle of the ultra wide angle system is more in line with formula (5), which makes the fisheye lens optical system have a planar image, which is more conducive to correcting system aberrations. Therefore, using equidistant projection imaging is more reasonable [14-17].

This scheme achieves the requirement of ultra wide angle for infrared warning equipment by reasonably allocating the optical mechanical structure, taking into account the efficiency of cold light, suppression of stray light, and system engineering.

3. System design and comparison

3.1 Requirements for optical system design

Technical characteristics and design requirements of infrared warning optical system Core features:

(1) Distortion control: Negative distortion needs to be introduced to match a limited image plane for a half field of view (>60 °), using non similar imaging to form barrel distortion, and using a fisheye lens to correct the image through an equidistant projection model; (2) Illuminance optimization: Compensate for edge illuminance decay through a negative vignex design, with only 40% edge illuminance when the half-field of view is 65°, and enhance the oblique beam flux by using the coma of the aperture of the retroactive structure; (3) Environmental adaptability: Meet the military wide temperature range thermal-free design requirements from -40 ° C to 60 ° C. (Experimental comparative analysis temperature range is -50 ° C to 70 ° C) ; (4) Performance evaluation: Emphasis on single-pixel angular resolution uniformity (target indication accuracy) and energy convergence degree (action distance).The design specifications for the optical system are shown in Table 1.

Table 1

Design indicators for the optical system section

Design Specifications	Design parameters
Working band	3.7 *um* ~ 4.8 *um*
Relative aperture	2.0
Field of view	≥ 95 °×95 °
Optical transmission	≥0.5@20lp/mm
System transmittance	≥85%
System distortion	≤2%
Energy concentration	≥0.8
Working mode	Optical passive thermal
Operating temperature	- 40 ℃ ~ 60 ℃
Barrel material	Aluminium alloy
Detector	640*512@25μm
Cold diaphragm efficiency	100%

3.2 Design of ultra-wide-angle one-shot imaging optical system

According to the above principles, the ultra-wide-angle single-imaging heat-free compact medium-wave cooled optical system designed in this system from left to right includes: light convergence group, thermal defocus compensation group, aberration correction group, detector window and its cold diaphragm. The basic structure of the system is shown in Fig. 4.

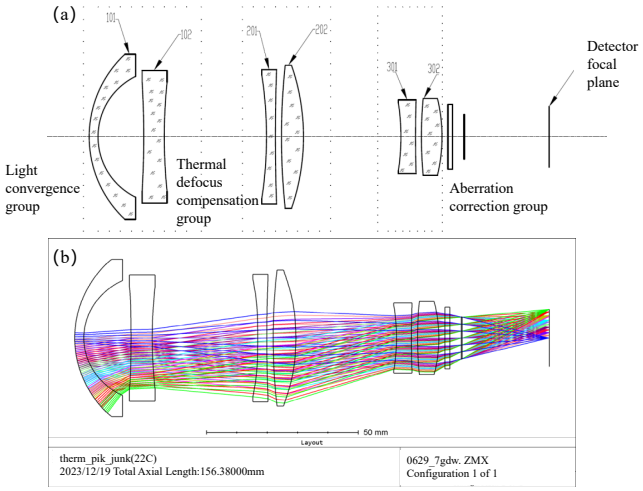

Fig. 4 Structure diagram of the infrared alert optical system

The light convergence group consists of a convex forward curved moon lens 101 and a double concave lens 102, which are responsible for converging the ultra wide area object side light into the thermal defocus compensation group. The curved moon lens 101 carries the receiving function of wide-angle incident light. At the same time, the hot defocus compensation group is composed of the double concave lens 201 and the convex lens 202, both of which are sulfur-based materials and have a certain compensating effect on the hot defocus generated by the system. Then, through the aberration correction group, it converges to the focal plane of the detector. The aberration correction group composed of concave lens 301 and the double convex lens 302 corrects the remaining aberrations, compresses the spatial envelope of the system and gives a unique advantage to the compactness of the system. To achieve a certain balance of aberrations at the focal plane of the detector. The system uses the above composition to achieve optical passive heat dissipation and compact shape envelope while meeting the ultra-wide Angle and making it more adaptable.

The air gap between the light convergence group and the thermal defocus compensation group is about 32mm, and the focal length ratio between them is 1:3. The air gap between the hot defocus compensation group and the aberration

correction group is about 30mm, and the focal length ratio between them is about 1:1.4. At the same time, the diaphragm of the system coincides with the cold diaphragm of the detector. The cold diaphragm efficiency of the system is 100%, which can better suppress the stray light of the system and improve the performance of the system.

Based on the three-level aberration theory, the system is balanced and optimized for aberrations according to the requirements of design parameters. The focal length of the system is 7.6mm; the field of view of the system is 120.6°×95.8°; the total length is 156.4mm; the full aperture of the first lens of the system is 60mm, and the relative aperture of the system is 2.

3.3 Design of ultra-wide-angle secondary imaging type optical system

The ultra-wide-angle secondary imaging heat-free compact medium-wave imaging system is shown in Fig.5. The system is balanced and optimized for aberrations based on the three-level aberration theory according to the design parameter requirements. The system focal length is 7.6mm; the system field of view is 123.4°×98.7°; the total length is 236.8 mm; the full aperture of the first lens of the system is 30 mm, and the relative aperture of the system is 2.

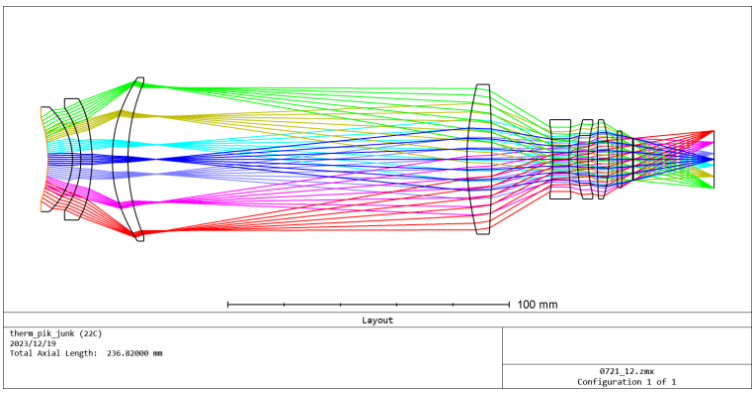

Fig. 5 Structure diagram of the secondary imaging type optical system

3.4 Comparison of primary and secondary imaging schemes

In the technological evolution of medium wave refrigeration infrared systems, the choice between primary imaging and secondary imaging has always been a focus of industry controversy and innovation. This not only involves engineering trade-offs in optical design, but also reflects the deep game of technical routes in different application scenarios.

A single imaging scheme, with its natural advantage of simple structure, often has a smaller length. The secondary imaging system, due to its intermediate

imaging surface, is longer than the primary imaging scheme, but has an advantage in terms of smaller lens aperture size. The relevant data will be included in the comparison of the subsequent schemes in this article (Table 4).

Both the primary and secondary imaging schemes use common combinations of silicon, germanium, and sulfur based glass, matched with aluminum alloy for material matching. This is a very common non thermal matching method, and by adding non spherical surfaces to infrared glass, most aberrations are corrected and deformation at high and low temperatures is converged. Through optical design optimization iterations, the system's performance at high and low temperatures tends to balance with that at room temperature, achieving the function of non thermal matching.

Furthermore, both the primary imaging and secondary imaging schemes use the first lens to capture the large field of view light into the system, acting as a "fish eye", and then compensate for aberrations through the subsequent lens group to achieve wide-angle function.

4. Imaging quality analysis

The modulation transfer function of an optical system is the core indicator that describes the system's ability to transmit spatial frequency information of objects, and it is also the most objective and quantitative tool for evaluating imaging quality. It breaks through the limitations of subjective evaluations such as traditional "resolution" and "clarity", and uses mathematical language to reveal the transmission laws of contrast and phase of optical systems for different details (spatial frequencies). It is widely used in lens design, imaging system optimization, and performance verification. In addition, system distortion rate is also an important indicator for evaluating imaging quality.

Option 1 (Design of Ultra Wide Angle One shot Imaging Optical System)

Table 2 shows the transfer function values of the primary imaging system extracted by the optical design software ZEMAX in three states: low temperature, room temperature, and high temperature.

Table 2

Theoretical transmission value of scheme 1 (Spatial Frequency 20 lp/mm**)**

Temperature (°C) Field (deg)		0	10	20	30	40	50	60	70	78.95
-55°C	Tangential	0.6594	0.6059	0.5620	0.6434	0.6452	0.5788	0.6576	0.7016	0.5640
	Sagittal	0.6594	0.6526	0.6581	0.7045	0.7492	0.7615	0.7608	0.7569	0.7122
22°C	Tangential	0.7696	0.7692	0.7531	0.7544	0.7365	0.6791	0.7109	0.7120	0.6946
	Sagittal	0.7696	0.7704	0.7699	0.7587	0.7240	0.6879	0.6751	0.7124	0.7381
70°C	Tangential	0.7350	0.7586	0.7653	0.7503	0.7404	0.6918	0.7189	0.7173	0.5924
	Sagittal	0.7350	0.7397	0.7405	0.7154	0.6646	0.6255	0.6202	0.6775	0.7241

From Table 2, it can be seen that when the logarithm of the optical transmission curve of the system is 20lp/mm, the optical transmission coefficient is greater than 0.5 at all temperature conditions, and the optical transmission coefficient at the edge field of view at room temperature is 0.6946.

Figs.6 shows the point sequence diagram of an imaging system in three states: low temperature, normal temperature, and high temperature.

Fig.6 (a) , (b) and (c) respectively represent the theoretical design point diagrams of the system at low temperature of -50°C, normal temperature of 22°C, and high temperature of 70°C

From Fig. 6, it can be seen that the column diagrams and Airy spot sizes of each field of view point in the imaging system are relatively close. Indicating that the system maintains relatively good image quality at different temperatures.

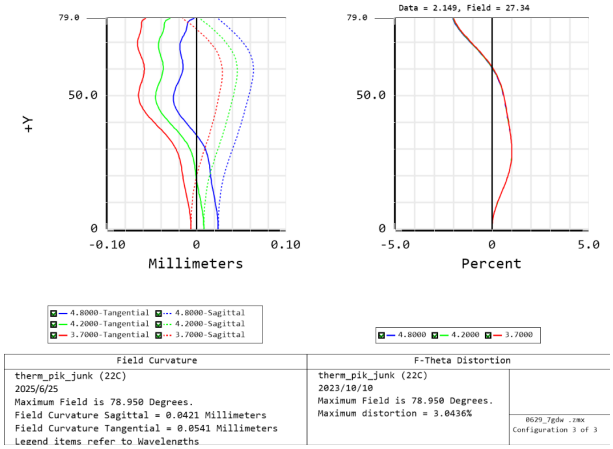

Fig. 7 System distortion curve

From Fig. 7, it can be seen that the F-theta distortion of the system in the entire field of view is less than 2%, which meets the system's usage requirements.

Option 2 (Design of Ultra Wide Angle Secondary Imaging Optical System)

Table 3 shows the transfer function values of the secondary imaging system extracted by the optical design software ZEMAX in three states: low temperature, room temperature, and high temperature.

Table 3

Theoretical transmission values of scheme 2 (Spatial Frequency 20 lp/mm**)**

Temperature (°C) Field (deg)		0	10	20	30	40	50	60	70	78.95
-55 °C	Tangential	0.6533	0.5796	0.6632	0.7129	0.7185	0.6859	0.6948	0.6911	0.5829
	Sagittal	0.6533	0.6632	0.7263	0.7337	0.7180	0.7064	0.7045	0.7278	0.5826
22° C	Tangential	0.7331	0.7157	0.7337	0.7359	0.7236	0.6931	0.7091	0.6788	0.6858
	Sagittal	0.7331	0.7307	0.6936	0.6355	0.6144	0.6220	0.6733	0.7377	0.6932
70° C	Tangential	0.7318	0.7218	0.7293	0.7347	0.7191	0.6784	0.6861	0.5904	0.6526
	Sagittal	0.7318	0.7277	0.6784	0.6159	0.5993	0.6125	0.6675	0.7373	0.6973

From Table 3, it can be seen that when the logarithm of the optical transmission curve of the system is 20lp/mm, the optical transmission coefficient is greater than 0.5 at all temperature conditions, and the optical transmission coefficient at the edge field of view at room temperature is 0.6858.

Fig.8 shows the dot plot of the secondary imaging system in three states: low temperature, room temperature, and high temperature.

Fig.8 (a) (b) and (c) respectively represent the theoretical design point diagrams of the system at low temperature of -50 ° C, normal temperature of 22 ° C, and high temperature of 70 ° C

From Fig.8, it can be seen that the column diagrams and Airy spot sizes of each field of view in the system are also relatively close, indicating that the image quality of each field of view in the system remains relatively good at different temperatures.

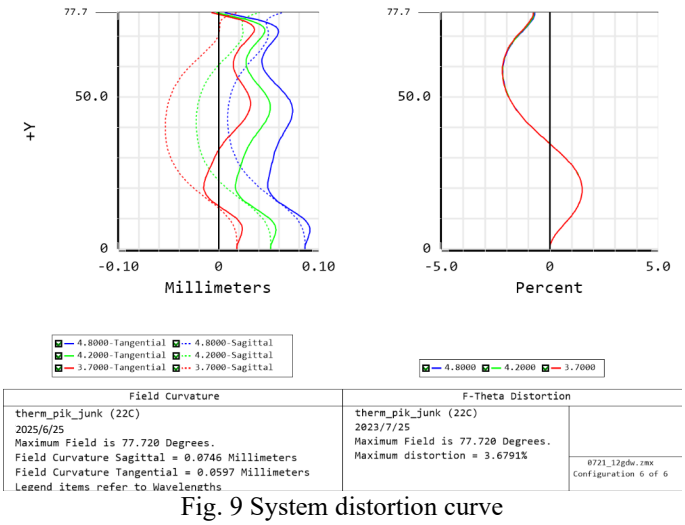

Fig. 9 System distortion curve

From the Fig.9, it can be seen that the maximum distortion of F-theta in the full field of view of the system is close to 2%, which can meet the system's

usage requirements.

Based on simulation analysis and theoretical calculations, structural design was carried out for the above two schemes, and their external dimensions are shown in Fig.10(a) and Fig.10(b), respectively.

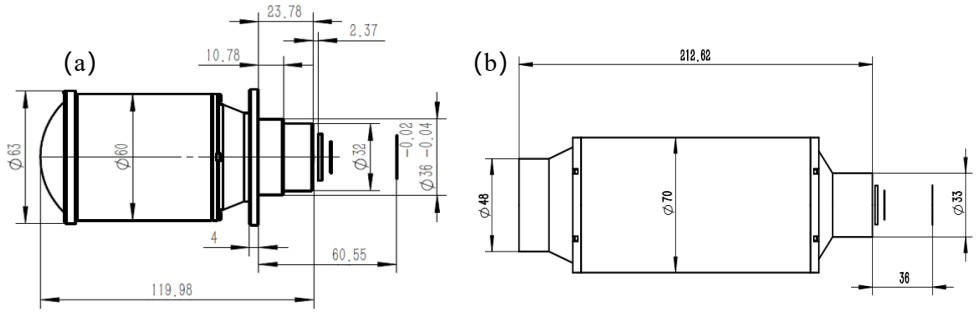

Fig.10 (a) Dimensions of the primary imaging lens, (b) External dimensions of secondary imaging lens

In order to compare the actual performance indicators of the two design schemes, the structural design of the lens component was carried out, and the physical production and assembly debugging of the parts were completed. The medium wave infrared cooling 640*512@25Aμm infrared camera component was connected to the lens, and the relevant indicators of the lens were tested.

Fig.11(a) shows a physical image of the lens for primary imaging, and Fig.11(b) shows a physical image of the lens for secondary imaging.

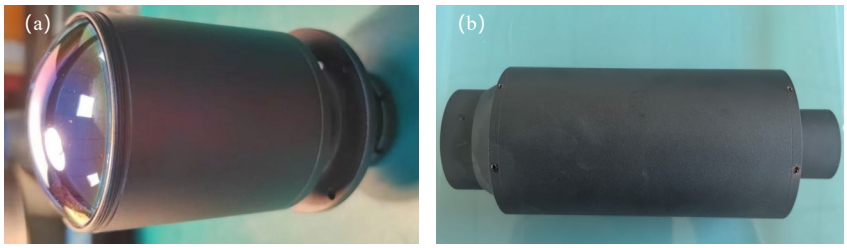

Fig. 11 (a) Physical image of a primary imaging lens, (b) Physical image of secondary imaging lens

Table 4

Comparison of the two imaging schemes

Metrics	One-time imaging scheme	Secondary imaging scheme
Focal length	The 7.6 mm	The 7.6 mm
Field of view	120.6°×95.8°	123.4°×98.7°
Aperture Number (F)	2	2
Optical transmission (20lp/mm)	0.65	0.60
Relative illuminance of the system	81%	80%
Distortion	1.9%	2%
Transmittance	86%	83%

System length	156.4mm	236.8mm
Headpiece caliber	60mm	30mm
Front window size	Φ120mm	Φ40mm

5. Conclusions

The system uses an anti-distant objective lens structure and an equidistant projection model to introduce a negative distortion compensation strategy (distortion ≤2%) and optical focal optimization allocation, and anultra-large field of view coverage of 120.6°×95.8° in a limited image plane (16mm×12.8mm) is achieved. Compared with traditional solutions, the field of view expansion rate is 38%. It achieves a focal plane offset of less than 5μm within a wide temperature range of -40 ° C to 60 ° C, allowing for stable imaging without focusing. Vibration resistance (vibration magnitude 5G) and sealing performance are enhanced through spacer ring fixation and edge sealing process. Experiments show that the cold diaphragm efficiency of the system is 100%; the edge illuminance uniformity is >80%, and the overall performance is better than similar multi-sensor splicing schemes. After the above comparative analysis, it can be concluded that the primary imaging scheme is superior to the secondary imaging scheme in terms of optical transmission, image distortion, system transmittance, system length, and other main indicators; Compared to the primary imaging optical scheme, the secondary imaging optical scheme only reduces the size of the front-end optical window, but it results in a relatively large system spatial envelope and a decrease in the system's transmittance. Therefore, considering all factors, the primary imaging optical scheme is selected as the optical scheme for this system.

Acknowledgement

Hunan Provincial Natural Science Foundation Project - Research and Application of Large Field Infrared Optical Imaging System (2024JJ7136);Key Project of Hunan Provincial Department of Education - Research on the regulation mechanism of single-source/multi-source ultrasound in improving segregation and eutectic microstructure segregation of aluminum ingots (24A0477).

REFERENCES

[1] *Abdelhakim, M. M., Khalil, A. A., Salah, A., & Alshershby, M.,* Exploring the impact of high-power infrared lasers on electro-optical systems performance: A field study with different wavelengths. Infrared Physics & Technology, vol. 139, pp. 105348, 2024. https://doi.org/10.1016/j.infrared.2024.105348

[2] *Shi, Z., Huang, M., Qian, L., Han, W., Zhang, G., & Lu, X.,* Unmanned Helicopter Airborne Fourier Transform Infrared Spectrometer Remote Sensing System for Hazardous Vapors Detection. Applied Sciences, vol. 14, no. 4, pp.1367, 2024. https://doi.org/10.3390/app14041367

[3] *Delleji, T., Slimeni, F., Ayadi, A., Lafi, M., &Chtourou, Z.,* Electro-Optical monitoring system for Early-Warning detection of Mini-UAVs. SN Computer Science, vol.6, no.6, pp.227, 2025. https://doi.org/10.1007/s42979-025-03756-1

[4] *Fang, J., Huang, K., Qin, R., Liang, Y., Wu, E., Yan, M., & Zeng, H.,* Wide-field mid-infrared hyperspectral imaging beyond video rate. Nature Communications, vol.15, no.1, pp.1811, 2024. https://doi.org/10.1038/s41467-024-46274-z

[5] *Tan, S., Wang, Y., Shi, G., Mu, S., Zhang, X., & Ma, L.,* Design and implementation of an integrated and rapidly assembled infrared three-band optical system. Astronomical Techniques and Instruments, vol. 2, no. 2, pp. 88-99, 2025. https://doi.org/10.61977/ati2024065

[6] *Choi, M., Park, J., Shin, J., Keawmuang, H., Kim, H., Yun, J., Rho, J.,* Realization of high-performance optical metasurfaces over a large area: a review from a design perspective. NpjNanophotonics, vol. 1, no. 1, pp.31, 2024. https://doi.org/10.1038/s44310-024-00029-2

[7] *Li, M., Gao, M., Wang, M., & Yang, F.,* Design and Experimental Study of Optical System for Ultra-Low Self-Heating Radiation Long-Wave Infrared Laser Communication Optical System. Journal of Russian Laser Research, vol.45, no.2, pp.174-183, 2024. https://doi.org/10.1007/s10946-024-10201-w

[8] *Wang, H., Zhou, Y., Jiang, X., Zuo, X., & Chen, M.,* Optimization of Thermal Control Design for Aerial Reflective Opto-Mechanical Structure. Sensors, vol.24, no. 4, pp. 1194, 2024. https://doi.org/10.3390/s24041194

[9] *Wang, B., Li, Y., Nie, Y., & Wang, Y.,* Design of spatial infrared freeform optical system with large field of view. Advanced Optical Manufacturing Technologies and Applications 2024; and Fourth International Forum of Young Scientists on Advanced Optical Manufacturing, vol.13280, pp.266-271, 2024. https://doi.org/10.1117/12.3047742

[10] *Vo, S. Q., Quan, P. V., & Bao, B. D.,* Global optimization methods for enhancing Fresnel lens design in passive infrared systems. Optics Continuum, vol.4, no.2, pp.409-420, 2025. https://doi.org/10.1364/OPTCON.550157

[11] *Sun, J.J.,* Design of long focal length terahertz optical system. Optical Review, vol.31, no. 4, pp.440-445, 2024. https://doi.org/10.1007/s10043-024-00901-8

[12] *Luo, X., Shi, Y., Guo, F., Hu, Y., Wang, L., Chen, Z., & Zhou, J.,* Design of a large imaging plane wide-band zoom adapter optical system for endoscopes. Optics Express, vol.33, no.2, pp.2809-2823, 2025. https://doi.org/10.1364/OE.550768

[13] *Kampe, T. U., Schmitt, S., Gristey, J. J., Harber, D., Pilewskie, P., Spuhler, P., Sutherland, T.,* Libera's wide-field-of-view camera for augmenting next-generation Earth radiation budget satellite observations. CubeSats, SmallSats, and Hosted Payloads for Remote Sensing VIII, SPIE, vol.13146, pp.5-18, 2024. https://doi.org/10.1117/12.3028338

[14] *Qin, X., Huang, W., Xu, M., & Jia, S.,* Research on the calibration method of a biomimetic polarized imaging system based on a camera projection model. Optics Continuum, vol.4, no.5, pp.1006-1029, 2025. https://doi.org/10.1364/OPTCON.549261

[15] *Song, Y., Zhang, T., & Qi, F.,* A correction method for calculating sky view factor in urban canyons using fisheye images. Building and Environment, vol.262, pp.111834, 2024. https://doi.org/10.1016/j.buildenv.2024.111834

[16] *Díaz, G. M., Lang, M., & Kaha, M.,* Simple calibration of fisheye lenses for hemispherical photography of the forest canopy. Agricultural and Forest Meteorology, vol.352, pp.110020, 2024. https://doi.org/10.1016/j.agrformet.2024.110020

[17] *Zakerinasab, Y., &Rezaei-Latifi, A.,* Athermalization of a type of fisheye optical system in the temperature range of Iran. Journal of Theoretical and Applied Physics, vol.18, no. 4, 2024. https://doi.org/10.57647/j.jtap.2024.1804.54